The performance of the EarthCARE cloud profiling radar in marine stratiform clouds

AGU PUBLICATIONS

JGR

Journal of Geophysical Research: Atmospheres

RESEARCH ARTICLE
10.1002/2016JD025090

Key Points:
- Spaceborne Cloud Profiling Radar observations of marine stratus clouds simulated
- Postprocessing techniques applied to improve range resolution and Doppler accuracy
- Effects of sampling rate, resolution, and clutter on detection, boundaries, and Doppler considered

Supporting Information:
- Supporting Information S1

Correspondence to:
D. Burns,
david.burns2@mail.mcgill.ca

Citation:
Burns, D., P. Kollias, A. Tatarevic, A. Battaglia, and S. Tanelli (2016), The performance of the EarthCARE Cloud Profiling Radar in marine stratiform clouds, *J. Geophys. Res. Atmos.*, *121*, 14,525–14,537, doi:10.1002/2016JD025090.

Received 14 MAR 2016
Accepted 15 NOV 2016
Accepted article online 18 NOV 2016
Published online 19 DEC 2016

The performance of the EarthCARE Cloud Profiling Radar in marine stratiform clouds

David Burns[1], Pavlos Kollias[1], Aleksandra Tatarevic[1], Alessandro Battaglia[2,3], and Simone Tanelli[4]

[1]Department of Atmospheric and Oceanic Sciences, McGill University, Montreal, Quebec, Canada, [2]National Centre for Earth Observation, University of Leicester, Leicester, UK, [3]Earth Observation Science, Department of Physics and Astronomy, University of Leicester, Leicester, UK, [4]Jet Propulsion Laboratory, California Institute of Technology, Pasadena, California, USA

Abstract Marine stratiform clouds are a challenging target for spaceborne radars due to their proximity to Earth's surface, limited vertical extent, and low radar reflectivity. The joint European-Japanese Earth Clouds, Aerosol and Radiation Explorer (EarthCARE) mission is scheduled for launch in 2019 and features the first atmospheric Cloud Profiling Radar (CPR) with Doppler capability in space. Here the performance of the CPR in (i) detecting these clouds and their boundaries and (ii) measuring the Doppler velocities of drizzle particles is evaluated. Extensive observations from the Atmospheric Radiation Measurement Mobile Facility in marine stratus regimes are used as input to an EarthCARE CPR simulator and to compare the resulting reflectivity factors, Doppler velocities, and cloud detections. Cloud detection of the CPR is 70–80% that of the ground-based radars, depending upon integration length and feature mask configuration. For clouds entirely contained within the surface clutter, detection is limited but is predicted to be an order of magnitude greater for the EarthCARE CPR than for CloudSat due to the improved range sampling rate of the former. The EarthCARE-CPR range resolution is found to introduce cloud top height and reflectivity biases of +100 m (equal to the range sampling rate) and +1.3 dB; by applying a constrained linear inversion to the range resolution, these are reduced to 30 m and 0.1 dB, respectively. The analysis indicates that a velocity uncertainty of 0.5 ms^{-1} is achievable through either a 5 km along-track integration or a combination of matched spatial filters and 1 km along-track integration.

1. Introduction

Marine stratiform clouds play a critical role in Earth's radiation budget and hydrological cycle and therefore in present and future climate model simulations. Their influence on Earth's climate can be attributed to their vast horizontal coverage, their ability to strongly reflect incoming shortwave radiation [*Hartmann et al.*, 1992], and their regulating effect on the marine boundary layer structure through drizzle and turbulence production [*Stevens et al.*, 2003]. Evaluation of marine stratus representation in climate models requires large-scale, long-term observational data sets. Such observations are challenging to conduct from ground-based platforms. Thus, spaceborne instruments, which provide global coverage, are key for monitoring the properties of marine clouds.

Earth Clouds, Aerosol and Radiation Explorer (EarthCARE) is a joint European Space Agency and Japanese Aerospace Exploration Agency satellite due to launch in 2019 that will carry a Cloud Profiling Radar (CPR), a high-spectral-resolution atmospheric lidar, a broadband radiometer, and a multispectral imager [*Illingworth et al.*, 2015]. Both independently and synergistically, these instruments will provide profiles of clouds, precipitation, and aerosol properties and top-of-atmosphere radiative fluxes and heating rates. EarthCARE may be considered the successor to the National Aeronautics and Space Administration (NASA) Afternoon Train, or A-Train, a formation of Earth Observing Satellites that carry a mix of active and passive remote sensing instruments. Among these are the Cloud Profiling Radar aboard CloudSat [*Stephens et al.*, 2008] and the Cloud-Aerosol Lidar with Orthogonal Polarization aboard Cloud-Aerosol Lidar and Infrared Pathfinder Satellite Observations [*Winker et al.*, 2009], which have, since their launches in 2006, provided extensive climatologies of marine boundary layer clouds [e.g., *Leon et al.*, 2008].

The 94 GHz EarthCARE CPR (EC-CPR) will feature several improvements over the CloudSat CPR (CS-CPR), including being the first spaceborne atmospheric radar with Doppler capabilities. This will allow it to provide

Table 1. Technical Characteristics of the EarthCARE and CloudSat Cloud Profiling Radars

Parameter	EC-CPR	CS-CPR
Frequency (GHz)	94	94
Altitude (km)	393 (mean)	705–732
Antenna diameter (m)	2.5	1.85
Pulse length (μs)	3.3	3.3
Range resolution (m)	500	485
Vertical sampling rate (m)	100	240
Along-track sampling rate (m)	500–1000	1100
Antenna beam width (deg)	0.095	0.12
PRF (kHz)	6.1–7.5	3.7–4.3
Sensitivity (dB*Z*)	−36	−30

information on not only cloud extent and structure but also vertical motions within clouds and precipitation. In addition to its Doppler capability, the EC-CPR employs a higher along-range sampling rate (100 m) and sensitivity (−36 dB*Z*) than the CloudSat CPR (CS-CPR) (240 m and −30 dB*Z*, respectively [*Tanelli et al*., 2008]). The enhanced sensitivity of the EC-CPR is primarily due to its lower flying altitude and larger antenna. A detailed comparison of the technical parameters of the two CPRs is given in Table 1. Despite these improvements, observations from spaceborne radars remain challenging. For instance, both the EC-CPR and CS-CPR use pulse lengths of 500 m, compared to below 50 m for typical ground-based radars [e.g., *Widener and Mead*, 2004; *Kollias et al*., 2007]. A longer pulse length is necessary for spaceborne radars to achieve sufficient sensitivity while operating at distances of hundreds of kilometers from their targets, but also reduces the range resolution, particularly in the absence of pulse compression. *Uttal and Kropfli* [2001] investigated the effect of long pulse lengths (450 m) in the context of spaceborne radar observations by artificially reducing the vertical resolution of ground-based radar data and found that this introduced an average reflectivity bias of +4 dB; note, however, that *Uttal and Kropfli* [2001] used nonweighted averaging across the 450 m pulse, while the range weighting functions of the CS-CPR and EC-CPR weight central reflectivities more heavily than those at pulse edges—as such, reflectivity biases in CS-CPR and EC-CPR data are likely smaller than those reported in *Uttal and Kropfli* [2001]. Vertical smoothing of CPR profiles also hampers the accurate definition of cloud boundaries; this is a particular problem for observations of marine stratiform clouds, which are thin (typically less than 500 m, the vertical resolution of the EC-CPR [*Wood*, 2012]) and therefore susceptible to proportionally large errors in cloud boundary estimates.

A further effect of the EC-CPR range resolution is that surface clutter—strong reflections of radar waves by the ground—extends into range gates up to 1 km above the ground. These surface echo signals can be several orders of magnitude stronger than hydrometeor signals, often causing observations of low-lying and low-reflectivity marine stratus clouds to be obscured or biased. Furthermore, precipitation-free marine strati typically have reflectivities close to or below the sensitivity of the EC-CPR, such that many of these clouds will go undetected even in the absence of surface clutter.

Spaceborne Doppler velocity measurements are affected by these and other factors. In low signal-to-noise ratio (SNR) conditions, random noise will dominate velocity estimates [*Kollias et al*., 2014]. In addition, the satellite's motion of 7 km s^{-1} combined with the EC-CPR antenna's beam width will both broaden the observed Doppler spectra and, in the case of nonuniform beam filling (NUBF), introduce biases that can reach several meters per second [*Kollias et al*., 2014; *Tanelli et al*., 2002; *Schutgens*, 2008]. Biases of similar magnitudes are produced by mispointing of the CPR antenna away from the nadir direction by even a few microrad [*Battaglia and Kollias*, 2015]. Together, these effects restrict the quality of the CPR reflectivity and Doppler estimates. However, postprocessing methods have the potential to mitigate these errors. For example, increased along-track integration can reduce random noise errors; reference targets with known velocities, such as the surface, allow correction for antenna mispointing; and NUBF errors can be corrected for with knowledge of the along-track reflectivity gradient.

The aims of this study are to quantify, in terms of biases and uncertainties, how well the EC-CPR captures (i) marine stratiform cloud morphology (i.e., reflectivity, cloud fraction, and cloud boundaries) and (ii) drizzle Doppler velocities. We also investigate the effectiveness of postprocessing techniques in reducing these measurement errors—specifically, a constrained linear inversion process, similar to those described in

Schutgens and Donovan [2004] and *Galati et al*. [1996], applied to the EC-CPR range resolution to retrieve a high-resolution reflectivity profile, and matched spatial filtering, following *Sy et al*. [2014], to reduce noise in the EC-CPR Doppler velocity field.

To address these questions, ground-based radar observations from two deployments of the U.S. Department of Energy Atmospheric Radiation Measurement (ARM) program [*Mather and Voyles*, 2013; *Stokes and Schwartz*, 1994] in marine stratus cloud regimes are used as input to an EC-CPR simulator. This outputs synthetic EC-CPR observations of the same scene, which can then be compared with the "true" ground-based data for a quantitative evaluation of the EC-CPR measurements. The simulator is also adapted to output CS-CPR observations to provide a direct comparison of the performance of the two spaceborne radars.

Details of the ground-based radar data and the simulator are presented in section 2. This includes the processing of the simulator output using a feature mask algorithm. In section 3, the simulated EC-CPR results are presented and compared with the simulator input data and simulated CS-CPR data. The effect of the surface echo, the horizontal sampling rate, the range resolution, and data processing techniques are discussed, as is the quality of the EC-CPR velocity estimation.

2. Simulator, Data, and Processing

2.1. Ground-Based Data

Observations from two recent deployments of the ARM Mobile Facility (AMF) are used [*Mather and Voyles*, 2013]. The first is the AMF-1 deployment at Graciosa Island, Azores (GRW) [*Rémillard et al*., 2012; *Wood et al*., 2015]. The second is the AMF-2 Marine ARM Global Energy and Water Cycle Experiment Cloud System Study Pacific Cross-section Intercomparison Investigation of Clouds (MAGIC), in which observations were carried out aboard the cargo ship Horizon Spirit during several trips between Los Angeles, CA, and Honolulu, HI [*Zhou et al*., 2015]. In both deployments, a vertically pointing 95 GHz W-band ARM Cloud Radar (WACR) [*Widener and Mead*, 2004] for GRW (and the Marine WACR (M-WACR) in the case of MAGIC) was deployed alongside several other instruments (e.g., ceilometer and microwave radiometer). The W-band radars provide estimates of radar reflectivity factor, mean Doppler velocity, and spectrum width. The WACR and M-WACR have sensitivities of -51 dBZ and -40 dBZ, respectively, the difference being due to their antenna sizes (1.2 m and 0.6 m) and integration times (2 s and 0.2 s). The two radars employ range sampling rates of 43 m and 21 m, respectively, although a pulse length of 300 ns is used by both.

Approximately 250 h of marine stratiform observations from the two AMF deployments are combined to produce statistics of the marine stratus scenes in order to evaluate the CPR measurements, although two example cases, one from each AMF deployment, are presented in detail [*Atmospheric Radiation Measurement (ARM) Climate Research Facility*, 2005, 2012]. The GRW case was observed on 29 November 2009 and the MAGIC case on 30 July 2013. Figure 1 displays the fields of reflectivity factor and Doppler velocity for the two scenes. Both contain drizzle-free and drizzling regions, with cloud thicknesses varying correspondingly from a few hundred meters (cloud only) to over a kilometer (cloud and drizzle), the latter often extending into the lowest 1 km above the surface. Reflectivity values vary from approximately 10 dBZ within strong drizzle patches to around -40 dBZ near cloud boundaries. Velocities are generally small, ranging from close to zero within clouds to magnitudes of 1–2 ms^{-1} in drizzle.

2.2. Simulator

The CPR simulator used in this study, described in detail in *Kollias et al*. [2014], produces CPR observations from ground-based and/or airborne radar data. Observed cloud scenes are first converted from a time-height field to an along-track height field using local wind speed soundings averaged over the cloud layer. The simulator then applies to the input data the effects of measurement by the EC-CPR, such as radar receiver noise; the horizontal and vertical resolutions; along-track integration; and, for the EC-CPR, spectrum broadening due to satellite motion and Doppler moment estimation that emulates the real-time onboard processing of EC-CPR signals. In *Kollias et al*. [2014], the focus was on high-level ice clouds, and thus, simulation of the surface return was not included. However, the surface echo is an important feature that restricts the detection of low-level clouds by spaceborne radars [*Tanelli et al*., 2008]; therefore, for this study, the surface echo is introduced in the simulator and is described here.

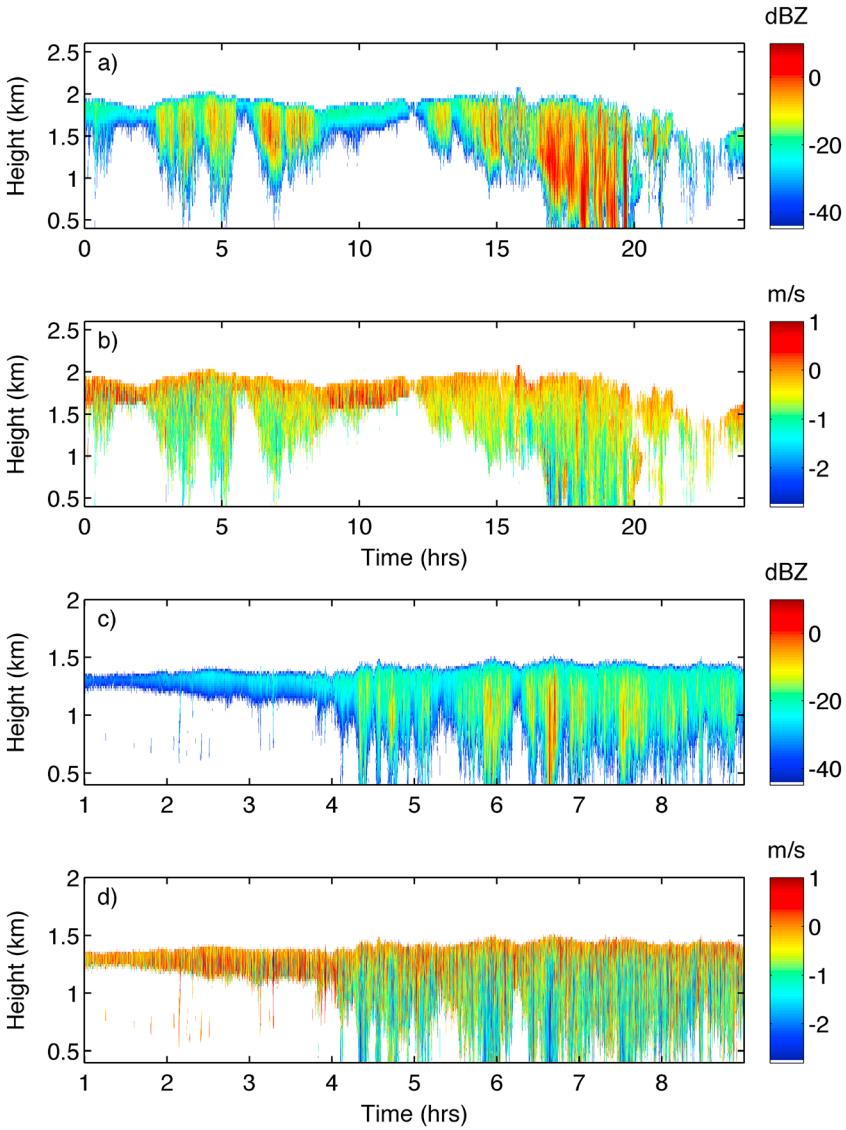

Figure 1. Time-height ARM radar observations of reflectivity factor and Doppler velocity for two AMF deployments in marine stratus regimes: (a and b) 30 July 2013 (MAGIC) and (c and d) 29 November 2009 (GRW). The upward (downward) vertical velocities are assumed positive (negative).

The profile of the surface echo is determined by the normalized cross section of the Earth's surface and the combined effect of the radar's range weighting function and receiver bandwidth. For the EC-CPR, a best approximation of the clear-sky surface return is produced by convolving the estimated point response function of the EC-CPR with the surface reflectivity. Variability of the surface return due to heterogeneous surface conditions, attenuation of the radar signal through the atmosphere, and changes in satellite altitude, which moves the surface's position within the range gate it intersects, have not been included in the EC-CPR simulator. This therefore constitutes a best-case scenario, where the only variation in the surface return is due to finite-sampling errors of the radar.

In the case of the CS-CPR, the average clear-sky surface return over ocean can be deduced from the CloudSat 2B-GEOPROF reflectivity product. However, to allow a comparison of the performance of the two radars under the same conditions, the EC-CPR surface echo profile is reused for the CS-CPR simulations. This is reasonable as the two radars share a similar pulse length and range weighting function (a comparison of the simulated EC-CPR and actual CS-CPR clear-sky reflectivity profiles, both after clutter reduction, is displayed in Figure 2). An ideal surface echo EC-CPR profile is also considered, in which the

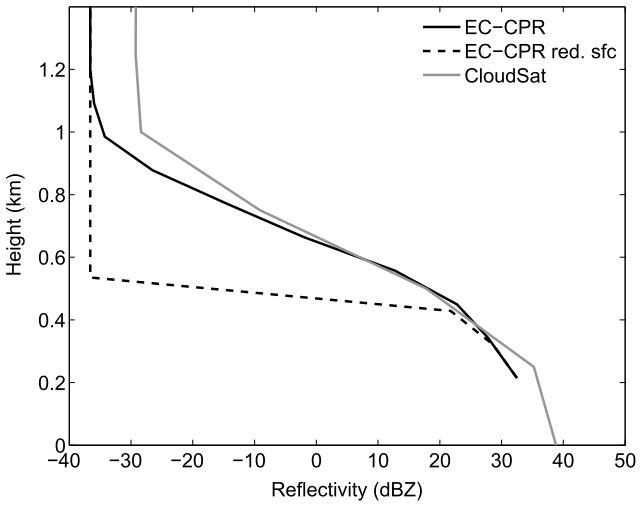

Figure 2. Actual CS-CPR and estimated EC-CPR average clear-sky surface return reflectivity profiles (after clutter and noise subtraction) and a reduced surface echo EC-CPR profile in which the clutter has been completely suppressed above 500 m.

surface clutter has been entirely suppressed above 500 m. This scenario is used to provide an upper bound to the EC-CPR receiver filter performance and to evaluate future spaceborne radar systems that could employ such ideal filters (contrasting with the aforementioned range resolution inversion and matched spatial filtering, which are readily applicable to EC-CPR data). This profile is also plotted in Figure 2. In the simulator, the mean Doppler velocity of the surface is assumed zero (valid under the condition that antenna mispointing has been sufficiently corrected for) and a narrow spectrum width (0.5 ms^{-1}) assigned, as the main contributor to Doppler spectral broadening is introduced later in the simulator. When concurrent (within the lowest 1 km), the WACR and surface clutter moments are combined to produce the total observed radar moments.

The simulator outputs estimates of reflectivity factor, mean Doppler velocity, and spectrum width based on pulse pair processing [*Doviak and Zrnic*, 1993] every 20–25 m of along-track displacement of the EC-CPR. These estimates are subsequently integrated horizontally to 500 m to reduce the impact of the receiver noise and satellite motion. Additional integration up to 10 km is performed in order to evaluate the quality of the measurements. The simulated Doppler velocities are corrected for NUBF according to the along-track reflectivity gradient method [*Kollias et al*., 2014].

2.3. Feature Mask and Processing

Since this study is concerned with the detection of weak targets often embedded in the surface clutter, it is necessary to introduce the feature mask (FM) detection algorithm that is similar to that proposed for the EC-CPR. The FM algorithm takes as input the raw-simulated EC-CPR signals described in section 2.2 and indicates sampling volumes which contain radar signal returns that are statistically significantly higher than the background signal (receiver noise, atmospheric noise, and surface clutter).

The first step in the FM is the calculation of the mean and standard deviation of the noise in echo-free (i.e., surface clutter- and cloud-free) returns within each EC-CPR profile. The *Hildebrand and Sekhon* [1974] method of noise estimation is used to determine these echo-free radar range gates. The mean +1, 2, or 3 standard deviations (hereafter referred to as 1–3σ) are then used as a dynamic threshold for hydrometeor detection in subsequent processing. Range gates in which the signal power is higher than the threshold are classified as significant and the rest as nonsignificant returns. The mean noise is then subtracted from the reflectivity profile. Extensive sensitivity tests that illustrate the effects of the choice of the threshold value are shown in section 3.

Surface clutter identification is the next step in the FM algorithm. Given the strength of the surface return relative to the background noise, range gates in approximately the lowest 1 km will be uniformly marked as significant in the previous step. In CloudSat data, surface clutter identification is performed by comparing the observed profile to a reference clear-sky profile. If the observed return power is above the 99th percentile of surface returns at that height, the signal at that range gate is classified as significant and the surface component of the signal is subtracted [*Marchand et al*., 2008; *Tanelli et al*., 2008]. Here a similar method is used, with average surface returns produced from clear-sky regions within each case. In each profile, if the signal power in a range gate is greater than the mean surface signal at that level +3 standard deviations of the surface signal, the volume is classified as significant; otherwise, the volume is marked as nonsignificant. The average surface profile is then subtracted.

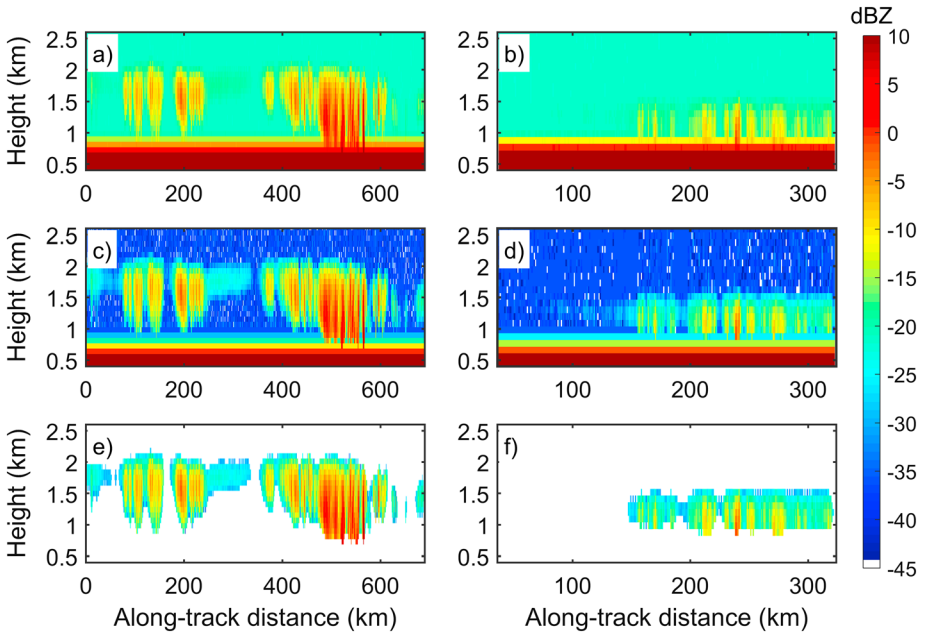

Figure 3. Simulated EC-CPR reflectivity fields of the (a, c, and e) GRW and (b, d, and f) MAGIC example cases: (Figures 3a and 3b) prior to any processing, (Figures 3c and 3d) after noise and clutter subtraction, and (Figures 3e and 3f) after application of the feature mask algorithm. Masked reflectivity fields are produced at a 1 km integration using a 3σ detection threshold.

Finally, a 2-D (along-track and along-range) filter is applied, similar to that used for CloudSat data [*Marchand et al*., 2008]. This runs a box, sized 3 by 3 resolution volumes, over the entire field [e.g., *Clothiaux et al*., 1995]. At each point, if more than half-plus-one of the surrounding volumes are classed as significant in the previous mask, then the central point is also marked as significant. If fewer than this are significant, the central point is classed as nonsignificant. This filter is applied iteratively twice primarily with the aim of reducing both false positives. Any volumes with a negative power are marked as nonsignificant. For simulated CS-CPR data, the mask procedure is adapted to match the 2B-GEOPROF mask described in *Marchand et al*. [2008]. Only mask values of 20, defined as a weak detection that may be an artifact of spatial correlation, or greater are used throughout the CS-CPR analysis in this study.

Following application of the FM algorithm, a range resolution inversion is applied to the reflectivity field to retrieve relatively high-resolution profiles. This process requires knowledge of the form of the EC-CPR range weighting function and range oversampling, as performed by the EC-CPR; as such, this technique is not applicable to CS-CPR data, which comprises a lower range sampling rate relative to its resolution. Matched spatial filters are applied to the EC-CPR Doppler velocity field as an alternative to along-track integration for the reduction of noise errors. The adaptive spatial filters are optimized for each cloud scene according to *Sy et al*. [2014]. The specifics of these techniques are described in the supporting information accompanying this article, and their results are discussed in section 3.

3. Results

Simulated EC-CPR reflectivity fields for the two sample cases (Figure 1) are depicted in Figure 3. The raw EC-CPR reflectivity field (prior to application of the FM algorithm), followed by the reflectivity after noise subtraction and surface clutter reduction, and finally the EC-CPR results after applying the FM algorithm are displayed in each column. The results in Figure 3 are produced using a 1 km horizontal integration and a significant detection threshold of 3σ. In both the GRW and MAGIC input reflectivity fields (Figure 1), there are many drizzle-free regions, characterized by relatively low reflectivities and thicknesses of only a few hundred meters. The signals here are generally close to or below the level of the noise and therefore are undetected in the masked EC-CPR result. Increasing the along-track integration (e.g., to 5–10 km) reduces the effective noise level, making many of these weak cloud signals detectable, though at the expense of a reduced horizontal resolution. Alternatively, the signal threshold for detection in the FM algorithm may be

Table 2. Detected Cloud Fraction of the EC-CPR and CS-CPR Relative to the Ground-Based WACR

Detection	EC-CPR 1 km, 1σ	EC-CPR 1 km, 2σ	EC-CPR 1 km, 3σ	CS-CPR
Estimated (%)	96	93	91	87
Actual (%)	79	73	68	47
No surface (%)	82	76	70	49
Surface only (%)	26	22	22	1

lowered while maintaining the integration length. Surface clutter can be seen in Figure 3 as the horizontal banding in the lowest 1 km of the nonmasked reflectivity fields. Even after surface clutter reduction (Figures 3c and 3d), below 700–800 m, the surface echo is stronger than the majority of the hydrometeor returns by several decibel. Subsequently, at these heights, the extraction of meteorological signals is challenging. The effects of the surface echo and feature mask configuration (integration length and significant detection threshold) on the EC-CPR-derived cloud statistics are evaluated in section 3.1.

3.1. Impact of Sampling Volume, Significant Detection Threshold, and Surface Echo

Cloud detection of the EC-CPR may be approximated as the proportion of WACR cloud profiles (averaged along track to the EC-CPR sampling rate) that have a maximum reflectivity greater than the EC-CPR sensitivity. However, this approach overestimates EC-CPR cloud detection by not accounting for the range resolution (which reduces peak reflectivities) and the limited range sampling rate. The estimated and actual cloud fractions of the EC-CPR and CS-CPR are given in Table 2 as percentages of the WACR cloud fraction. The actual detections are significantly lower than those estimated using a reflectivity threshold. This effect is amplified for the CS-CPR, which features the same range resolution as the EC-CPR but a lower range sampling rate. It is important to note that, because these results are produced relative to the WACR, they do not account for clouds that are undetected by the ground-based radars but that may be detected through, e.g., lidar observations.

The effect of the surface echo on detected cloud fraction is analyzed by separating profiles into those in which the cloud is entirely immersed in the surface returns (i.e., WACR cloud top height is lower than 1 km) and those at least partially above the surface clutter. The EC-CPR detects between one fifth and one quarter of the clouds located entirely within the lowest 1 km; due to the simplifications made during the simulation of the surface clutter, this is likely larger than the value in actual observations. However, under the same favorable simulated surface conditions, CS-CPR detection of these clouds is an order of magnitude smaller than that of the EC-CPR, again an effect of the restricted range sampling rate of the former. For the idealized surface clutter simulations in which clutter is suppressed above 500 m, EC-CPR detection of clouds in the lowest 1 km is virtually equal to that of clouds with cloud top above 1 km, as almost no clouds are entirely below 500 m.

Similar detections to the 1 km, 1σ FM configuration may be achieved using a 10 km integration and a 3σ detection threshold. However, this results in a coarser resolution not suitable for many cloud types and increases the risk of false detections; for a 1 km, 1σ mask, false detections (defined as profiles in which the EC-CPR, but not the WACR, detects hydrometeors) are virtually zero, but this increases to approximately 3% of all cloud-containing profiles when a 10 km, 3σ configuration is used. This is attributed primarily to the extended along-track integration that fills in breaks between clouds. While the results of Table 2 confirm that a lower a EC-CPR detection threshold is preferable for increased detection, the FM configuration also impacts the accuracy of EC-CPR cloud boundary and reflectivity estimates. This is illustrated in Figures 4 and 5.

Figure 4 displays the distributions of cloud thickness measured by the ground-based radars and the EC-CPR in the GRW and MAGIC campaigns, separated into drizzling and nondrizzling profiles. The presence of drizzle within a profile is determined with a height-dependent reflectivity threshold following *Wang and Geerts* [2003]. To allow direct comparisons of the unnormalized distributions, the WACR data are averaged along track to the 500 m EC-CPR sampling rate with EC-CPR data at longer integrations oversampled to the same rate. The EC-CPR distributions are produced using 1σ and 3σ thresholds at a 1 km integration and a 3σ threshold at a 10 km integration. The idealized surface clutter simulated data uses a 1 km integration and a 3σ threshold. The ground-based radar drizzle-free distributions (Figures 4a and 4c) are centered on thicknesses of approximately 500 m, with a significant number of profiles having

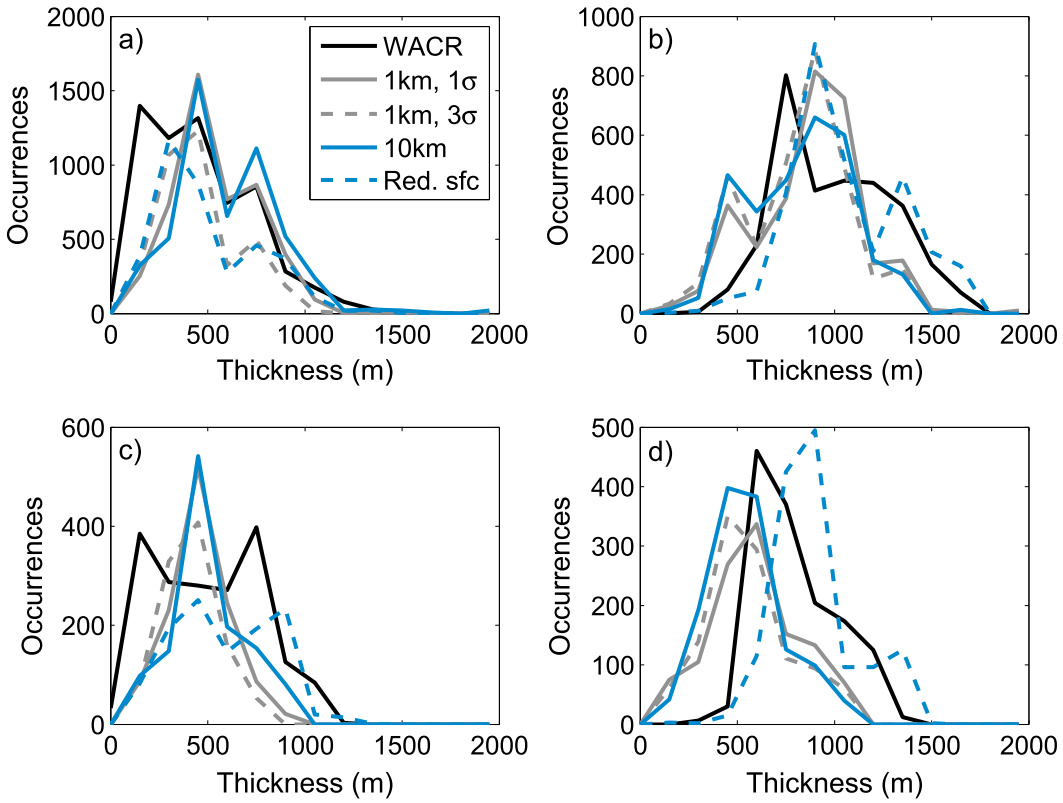

Figure 4. Probability density functions of cloud thickness as measured by WACR and EC-CPR in (a) GRW drizzle-free profiles, (b) GRW drizzling profiles, (c) MAGIC drizzle-free profiles, and (d) MAGIC drizzling profiles. PDFs are constructed by sampling all data to 500 m along track.

thicknesses less than this. The EC-CPR, in all configurations, underrepresents these clouds due to the stretching effect of the EC-CPR range resolution. This effect is slightly weaker in the 1 km, 3σ distributions due to the compensating effect of the reduced sensitivity, which means that cloud boundaries are often below the level of the noise.

The distributions of drizzling clouds are broader, particularly for the GRW campaign (Figure 4b), where thicknesses reach almost 2 km, compared to below 1.5 km for MAGIC (Figure 4d). Here the best fit to the WACR data is achieved by the reduced surface simulation data, with all other distributions biased toward lower thickness values. This indicates that the surface clutter obscures cloud base in drizzling profiles (as is seen in Figure 3), leading to an overrepresentation of shallow drizzling clouds. In both drizzling and nondrizzling profiles, the accuracy of the EC-CPR-derived cloud top height (defined as the midpoint of the highest range bin within a cloud layer) is calculated (with the WACR cloud top averaged to 500 m along track, the initial sampling rate of the EC-CPR, and the EC-CPR data oversampled to this rate). As with cloud fraction, this depends upon the value of the FM detection threshold. Using a 1 km along-track integration and 3σ threshold, the root-mean-square error (RMSE) is 91 m and the bias is 58 m (an overestimation by the EC-CPR). Using the same integration length and a 1σ threshold, the values are 128 m and 106 m, respectively; i.e., when a 1σ threshold is in use, the cloud top overestimation bias is comparable in magnitude to the range sampling rate of the EC-CPR (100 m). The improvement in cloud top accuracy attained using a 3σ threshold is the result of a cancellation of errors, in which the stretched boundaries (which have relatively low reflectivities) are below the sensitivity of the higher significant detection threshold. Accordingly, the CS-CPR cloud top estimates contain an average bias of just 36 m due to the radar's reduced sensitivity relative to the EC-CPR 3σ threshold (although the coarse sampling rate of the CS-CPR produces an RMSE of 139 m, larger than the EC-CPR values). While beneficial in this instance, such a cancellation of errors should not be relied upon as a matter of course; instead, the EC-CPR errors may be reduced by applying the range resolution inversion process (to the 1 km, 1σ reflectivity field). In profiles where the conditions for the application of the algorithm are met

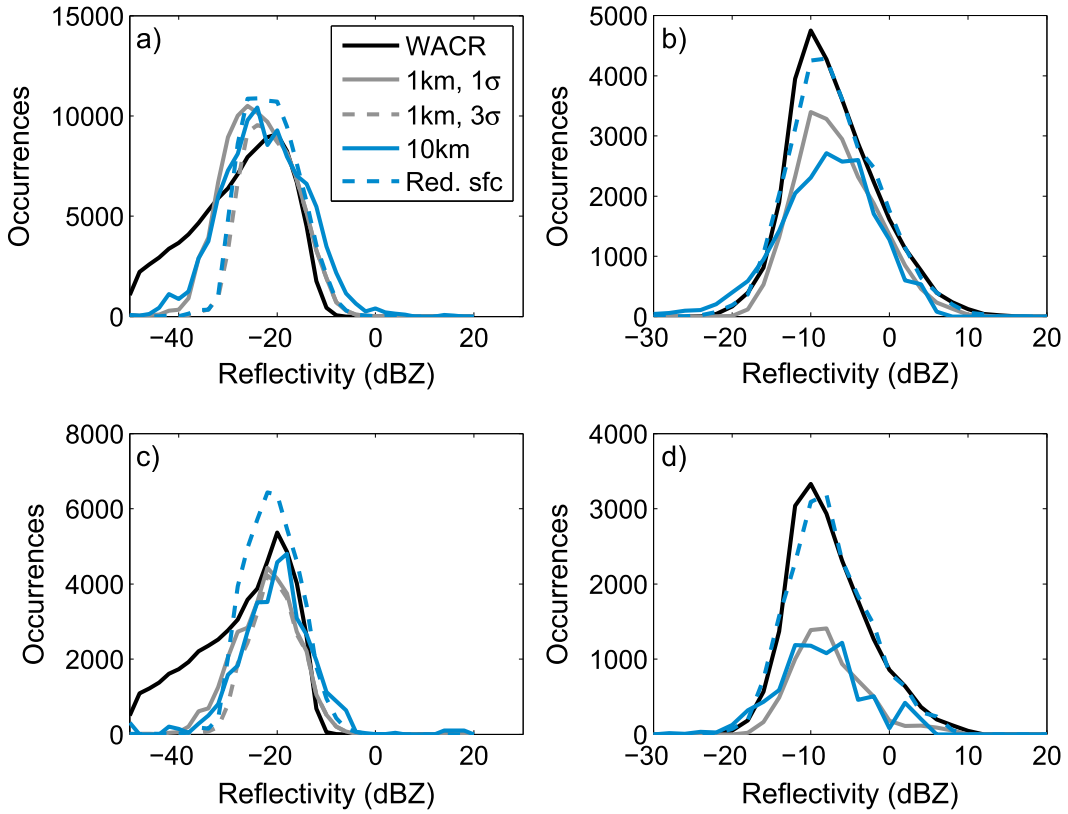

Figure 5. Probability density functions (PDFs) of reflectivity as measured by WACR and EC-CPR in (a) GRW drizzle-free volumes, (b) GRW drizzling volumes, (c) MAGIC drizzle-free volumes, and (d) MAGIC drizzling volumes. PDFs are constructed by sampling all data to 500 m along track and WACR vertical sampling.

(approximately one quarter of all profiles containing hydrometeor signals; detailed in supporting information), the average RMSE and bias are reduced from 140 m and 124 m to 62 m and 33 m, respectively.

The WACR and EC-CPR distributions of reflectivity factor are shown in Figure 5, separated by campaign and for drizzling and nondrizzling radar sampling volumes. For comparison purposes, the data are sampled along track to the 500 m EC-CPR initial grid and vertically to the WACR range sampling rate. In volumes containing drizzle (Figures 5b and 5d), WACR reflectivities peak at approximately −10 dBZ in the ground-based radar distributions, and this is well matched by the EC-CPR in all configurations (the choice of significant detection threshold has no effect in high SNR drizzling volumes so the 1 km, 3σ distribution is not included in Figures 5b and 5d). The total number of detected drizzling volumes is lower for the EC-CPR in all except the reduced surface simulations due to the masking effect of the surface clutter in the lowest 1 km. In nondrizzling volumes (Figures 5a and 5c), the location of the peak reflectivity (around −20 dBZ) is again reproduced by the EC-CPR; however, greater reflectivities (−10 dBZ and above) are overrepresented in the EC-CPR distributions. This is an effect of the EC-CPR resolution, both along track and along range, which introduces strong drizzle signals into cloud-only volumes. At lower reflectivities, the effect of an increased integration or lower significant detection threshold on the EC-CPR sensitivity can be seen, which allows more low-reflectivity features to be captured relative to the least sensitive (1 km, 3σ) configuration. However, the ground-based radar distributions contain reflectivity values of −40 dBZ and below, which the EC-CPR is not able to capture in any FM configuration tested here.

The average deviation between the EC-CPR and WACR reflectivity factor values is calculated (in logarithmic units): at a 1 km horizontal integration and 3σ threshold, the bias is 2.1 dB (an overestimate by the EC-CPR) and the RMSE is 5.9 dB, with very similar values present when using a 1σ threshold at the same along-track integration. The primary sources of these errors, which are calculated by oversampling the EC-CPR data to the WACR grid, are the range and along-track resolution of the EC-CPR, which introduce strong drizzle signals into the surrounding low-reflectivity cloud, with biases of more than 10 dB often present in the uppermost

Table 3. Average EC-CPR Velocity RMSEs at a Range of Integrations, With and Without the Application of Matched Spatial Filters

PRF (kHz)	500 m Integration [No NUBF Correction] (m/s)	1 km Integration [No NUBF Correction] (m/s)	5 km Integration [No NUBF Correction] (m/s)	500 m Matched Spatial Filters (m/s)	1 km Matched Spatial Filters (m/s)	5 km Matched Spatial Filters (m/s)
6.5	1.79 [2.02]	1.22 [1.51]	0.59 [0.70]	0.63	0.57	0.50
7.0	1.66 [1.96]	0.97 [1.37]	0.49 [0.59]	0.61	0.53	0.47
7.5	1.54 [1.85]	0.82 [1.29]	0.48 [0.60]	0.66	0.52	0.46

portions of drizzling clouds. After averaging the WACR data along track to the EC-CPR horizontal resolution (including both along-track integration and antenna pattern resolution), the average EC-CPR bias is 1.3 dB (1σ threshold), which is attributable to the range resolution (the introduction of a net bias due to averaging is explained by the fact that the logarithm of a linear average is always greater than the average of the logarithms). As with the cloud top overestimation bias, this may be reduced through the application of a range resolution inversion. In profiles in which this is applied, the average bias and RMSE are reduced from 1.2 dB and 4.8 dB to 0.1 dB and 4.1 dB, respectively. The remaining uncertainty is a mix of range resolution, noise, and surface clutter residuals.

3.2. Drizzle Doppler Velocity

Average EC-CPR velocity RMSEs across all GRW and MAGIC cases are calculated for a range of along-track integrations, with and without the application of matched spatial filters (Table 3). Errors are estimated by integrating the WACR velocities along track to 500 m, the initial sampling rate of the EC-CPR, and oversampling the EC-CPR data at other integrations to this grid. EC-CPR volumes with SNR less than 0 dB are excluded from these calculations, as are range gates below 1 km (due to the influence of the surface clutter). At a midrange pulse repetition frequency (PRF) value of 7.0 kHz, along-track integrations of 1 km and 5 km produce average errors of 0.97 ms^{-1} and 0.49 ms^{-1}, respectively (after correction for NUBF biases). The former is comparable in magnitude to typical Doppler velocities in drizzle, suggesting that a minimum along-track integration of 5 km is necessary to produce reasonable uncertainties. However, increased along-track integration reduces the ability of the EC-CPR to represent the true variability of the velocity field; this is seen in Figure 6, which compares EC-CPR and WACR velocity fields for a portion of the GRW example case.

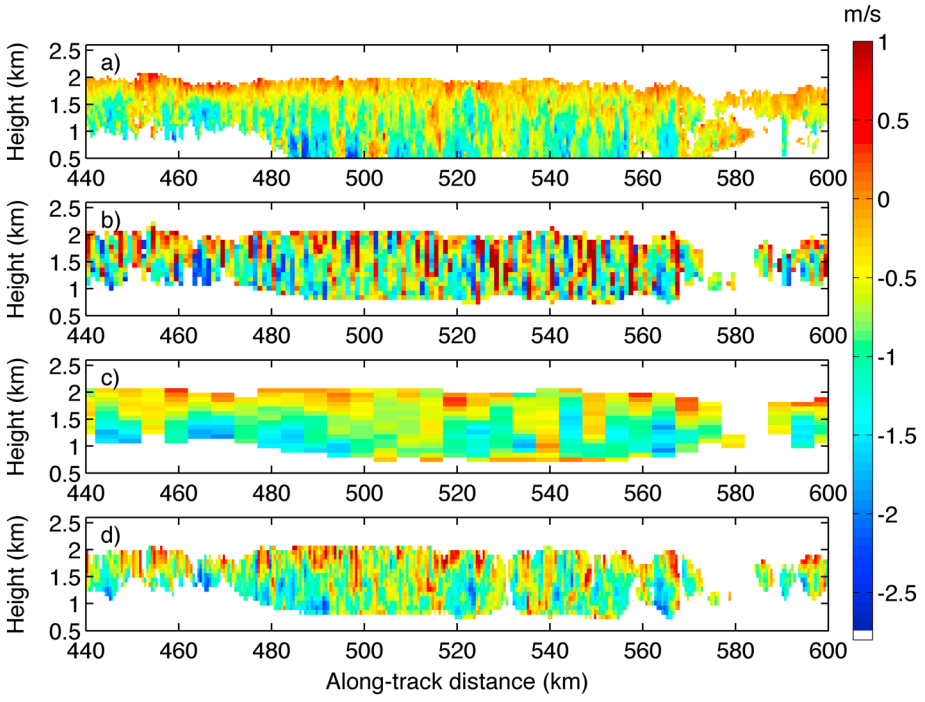

Figure 6. Along-track height velocity fields for a section of GRW example case, as measured by (a) WACR and EC-CPR at (b) 1 km integration, (c) 5 km integration, and (d) 500 m integration with matched filtering.

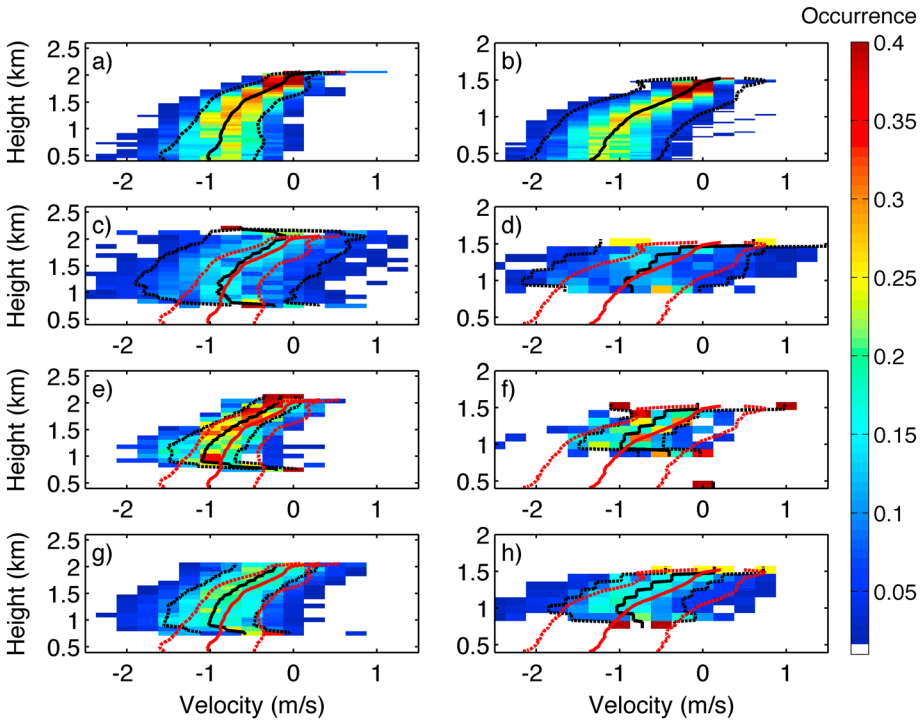

Figure 7. Joint histograms of Doppler velocity (0.25 ms^{-1} bin width) versus height for GRW and MAGIC example cases, measured by (a and b) WACR and EC-CPR at (c and d) 1 km integration, (e and f) 5 km integration, and (g and h) 500 m integration with matched spatial filters applied. The solid and dashed lines show the mean velocity ±1 standard deviation as a function of height, with WACR plots reproduced in red over EC-CPR histograms.

Alternatively, matched filtering of the EC-CPR velocity field produces uncertainties of 0.61 ms^{-1} at the initial 500 m sampling rate (PRF of 7.0 kHz), which may be reduced to 0.53 ms^{-1} through subsequent integration to 1 km. This is comparable to that achieved through a standard 5 km along-track integration while better preserving the horizontal resolution of the EC-CPR. These uncertainties are slightly worse than the 0.5 ms^{-1} at the 500 m sampling rate reported in *Sy et al.* [2014], achieved using the same method of filter optimization. In *Sy et al.* [2014], however, a range of cloud types (e.g., stratiform rain, snowstorms, and cirrus and cumulus clouds) were considered, as opposed to stratiform clouds in this study; this affects the true EC-CPR velocity error (as a combination of random noise, NUBF residuals, range resolution errors, etc.) and thus the performance of the filters.

It is not immediately apparent what causes the increase in the 500 m filtered velocity error when the PRF is increased from 7.0 kHz to 7.5 kHz or why this increase is reversed after subsequent integration to 1–5 km. A possible explanation for the former is that the method of filter optimization described in *Sy et al.* [2014] relies on the assumption that random noise is the only error source in the EC-CPR velocity field. If other error sources are negligible, this assumption is approximately valid and the filter performs well. However, as other sources of error become proportionally larger (i.e., when PRF is increased and the random noise errors decrease), this assumption breaks down and the filter matching method is less appropriate. This would also explain the relatively small increase in uncertainty when decreasing the PRF from 7.0 kHz to 6.5 kHz (compared to the equivalent change in error of the 5 km integration, nonfiltered velocity field), as the changes in filter optimization and random noise partially cancel out.

The 5 km integration velocity field also sees a smaller than expected error reduction after the PRF is increased from 7.0 kHz to 7.5 kHz. As with the filtered velocity fields, this is likely due to there being several sources of velocity uncertainty. Changes to PRF influence the random noise component of the velocity error but not NUBF residuals or range resolution errors, giving rise to a lower limit to the velocity uncertainty that depends upon the EC-CPR resolution and the variability within the cloud scene.

Velocity-height relations of the WACR and EC-CPR velocity fields for the GRW and MAGIC example cases are shown in Figure 7. The EC-CPR velocities in Figure 7 are produced using 1 km and 5 km along-track integrations and a 500 m integration with matched spatial filters applied. In both cases, the WACR velocities (Figures 7a and 7b) show similar relations with height. At cloud top, velocities tend toward zero. Toward cloud base, the mean velocity decreases to approximately 1 ms^{-1} at 500 m, where drizzle dominates the mean reflectivity-weighted velocity. The EC-CPR tends to overestimate the mean velocity in all cases due to it being a reflectivity-weighted velocity average, with higher reflectivities generally indicating larger droplets and therefore larger fall speeds. This effect is most prevalent in the 5 km integration profile, indicating that, for direct comparison with average velocity profiles of ground-based radars, higher resolution (i.e., shorter integration) data may be preferable despite the corresponding increase in variation about the mean. In the lowest 1 km, EC-CPR velocities are biased to zero due to the surface's stationary velocity and strong reflectivity, reducing the usefulness of velocities within these range gates.

4. Conclusions

Global observations of marine stratiform clouds are key to improve our understanding of these cloud systems and subsequently improve their representation and feedback in future climate simulations. The upcoming EarthCARE CPR, scheduled to launch in 2019, is expected to continue and expand the observational record of the NASA CloudSat CPR. The EC-CPR features several improvements over the CS-CPR, including a higher range sampling rate, increased sensitivity, and the addition of Doppler capability. Here ground-based radar observations of marine stratiform clouds are used as input to an EC-CPR simulator, and the ability of the EC-CPR to detect marine stratocumulus clouds, retrieve their boundaries, and measure their Doppler velocities is evaluated. A range resolution inversion technique and matched spatial filtering of Doppler velocities are tested as possible methodologies of reducing EC-CPR measurement errors.

Along-track integration and the choice of threshold for detection in the FM algorithm are found to significantly impact EC-CPR cloud detection and boundary accuracy. The EC-CPR detects between 70 and 80% of the clouds detected by the ground-based WACRs depending on integration length and significant detection threshold; this is significantly lower than would be predicted by applying a sensitivity threshold to the ground-based data due to the effect of the EC-CPR range resolution and sampling rate. For clouds contained entirely in the lowest 1 km, EC-CPR detection is limited, although it is found to be an order of magnitude greater than CS-CPR detection of the same clouds.

The coarse range resolution of the EC-CPR introduces significant errors to derived cloud boundaries, particularly when compared to the shallow thickness of these cloud systems. Using a 1σ detection threshold, EC-CPR cloud top contains an average overestimation bias comparable to the radar's range sampling rate of 100 m and an RMSE of 130 m. If a 3σ detection threshold is used, these values are slightly lower at 60 m and 90 m, respectively. The range resolution also introduces an average reflectivity bias of 1.3 dB (at a 1 km integration and either significant detection threshold). By applying a constrained linear inversion to the EC-CPR range resolution, the aforementioned biases are reduced to 30 m (1σ detection threshold) and 0.1 dB, respectively. However, the resolution inversion is limited in its applicability by surface clutter and noise, such that it may be applied in only one quarter of clouds in this data set. The conditions for application should be met more regularly in higher, thicker clouds such as cirrus.

Horizontal integration of 5 km is found to be necessary to reduce the average EC-CPR Doppler velocity error to approximately 0.5 ms^{-1}, while integration of 1 km produces errors of close to 1 ms^{-1}. These errors are not negligible when compared with average velocity magnitudes of 1 ms^{-1} within drizzling clouds. By applying matched spatial filters to the EC-CPR Doppler velocity field, uncertainties of 0.6 ms^{-1} are achievable while preserving the EC-CPR initial sampling rate of 500 m or 0.5 ms^{-1} by integrating the filtered velocity field along track to 1 km. Velocities within the lowest 1 km are biased toward zero by the stationary surface return and are therefore limited in their value.

Acknowledgments
This work was supported by the European Space Agency under the Doppler Radar and Synergy Products for EarthCARE project. The contributions by Simone Tanelli were performed at the Jet Propulsion Laboratory, California Institute of Technology, under contract with the National Aeronautics and Space Administration. Support by the NASA US Participating Investigator Program is gratefully acknowledged. The ARM WACR and ceilometer data were acquired from the ARM data archive. CloudSat CPR data were acquired from the CloudSat Data Processing Center. Figures and simulated data used in this study are available at http://meteo.mcgill.ca/~dburns/EC_CPR_sim_data.tar.gz.

References

Atmospheric Radiation Measurement (ARM) Climate Research Facility (2005), Updated hourly. W-band (95 GHz) ARM Cloud Radar (WACR). 2009-11-22 to 2010-07-06, 39.0911 N 28.0297 W: ARM Mobile Facility (GRW) Graciosa Island, Azores, Portugal; AMF1 (M1). Compiled by N. Bharadwaj, D. Nelson, B. Isom, J. Hardin, I. Lindenmaier, K. Johnson and A. Matthews. Atmospheric Radiation Measurement (ARM) Climate Research Facility Data Archive: Oak Ridge, Tennessee, USA. Data set accessed 2014-03-18 at doi:10.5439/1025317.

Atmospheric Radiation Measurement (ARM) Climate Research Facility (2012), Updated hourly. Marine W-band (95 GHz) ARM Cloud Radar (MWACR). 2013-07-16 to 2013-08-11: ARM Mobile Facility (MAG) Los Angeles, CA to Honolulu, HI - container ship Horizon Spirit; AMF2 (M1). Compiled by N. Bharadwaj, K. Johnson, B. Isom, J. Hardin and A. Matthews. Atmospheric Radiation Measurement (ARM) Climate Research Facility Data Archive: Oak Ridge, Tennessee, USA. Data set accessed 2014-06-11 at doi:10.5439/1150242.

Battaglia, A., and P. Kollias (2015), Using ice clouds for mitigating the EarthCARE Doppler radar mispointing, *IEEE Trans. Geosci. Remote Sens.*, *53*(4), 2079–2085, doi:10.1109/TGRS.2014.2353219.

Clothiaux, E. E., M. A. Miller, B. A. Albrecht, T. P. Ackerman, J. Verlinde, D. M. Babb, R. M. Peters, and W. J. Syrett (1995), An evaluation of a 94-GHz radar for remote sensing of cloud properties, *J. Atmos. Oceanic Technol.*, *12*(2), 201–229, doi:10.1175/1520-0426(1995)012<0201:AEOAGR>2.0.CO;2.

Doviak, R. J., and D. S. Zrnic (1993), *Doppler Radar and Weather Observations*, 2nd ed., Academic, San Diego, Calif.

Galati, G., M. Naldi, and M. Ferri (1996), Reconstruction of the spatial distribution of radar reflectivity of precipitation through linear-inversion techniques, *IEE Proc. Radar Sonar Navig.*, *143*(6), 375–382, doi:10.1049/ip-rsn:19960722.

Hartmann, D. L., M. E. Ockert-Bell, and M. L. Michelsen (1992), The effect of cloud type on Earth's energy balance, *J. Clim.*, *5*, 1281–1304, doi:10.1175/1520-0442(1992)005<1281:TEOCTO>2.0.CO;2.

Hildebrand, P. H., and R. S. Sekhon (1974), Objective determination of the noise level in Doppler spectra, *J. Appl. Meteorol.*, *13*(7), 808–811, doi:10.1175/1520-0450(1974)013<0808:ODOTNL>2.0.CO;2.

Illingworth, A. J., et al. (2015), The EarthCARE satellite: The next step forward in global measurements of clouds, aerosols, precipitation, and radiation, *Bull. Am. Meteorol. Soc.*, *96*(8), 1311–1332, doi:10.1175/BAMS-D-12-00227.1.

Kollias, P., E. E. Clothiaux, M. A. Miller, E. P. Luke, K. L. Johnson, K. P. Moran, K. B. Widener, and B. A. Albrecht (2007), The Atmospheric Radiation Measurement Program Cloud Profiling Radars: Second-generation sampling strategies, processing, and cloud data products, *J. Atmos. Oceanic Technol.*, *24*, 1199–1214, doi:10.1175/JTECH2033.1.

Kollias, P., S. Tanelli, A. Battaglia, and A. Tatarevic (2014), Evaluation of EarthCARE Cloud Profiling Radar Doppler velocity measurements in particle sedimentation regimes, *J. Atmos. Oceanic Technol.*, *31*(2), 366–386, doi:10.1175/JTECH-D-11-00202.1.

Leon, D. C., Z. Wang, and D. Liu (2008), Climatology of drizzle in marine boundary layer clouds based on 1 year of data from CloudSat and Cloud-Aerosol Lidar and Infrared Pathfinder Satellite Observations (CALIPSO), *J. Geophys. Res.*, *113*, D00A14, doi:10.1029/2008JD009835.

Marchand, R., G. G. Mace, T. Ackerman, and G. Stephens (2008), Hydrometeor detection using CloudSat—An Earth-orbiting 94-GHz cloud radar, *J. Atmos. Oceanic Technol.*, *25*(4), 519–533, doi:10.1175/2007JTECHA1006.1.

Mather, J. H., and J. W. Voyles (2013), The ARM Climate Research Facility: A review of structure and capabilities, *Bull. Am. Meteorol. Soc.*, *94*(3), 377–392, doi:10.1175/BAMS-D-11-00218.1.

Rémillard, J., P. Kollias, E. Luke, and R. Wood (2012), Marine boundary layer cloud observations in the Azores, *J. Clim.*, *25*(21), 7381–7398, doi:10.1175/JCLI-D-11-00610.1.

Schutgens, N. A. J. (2008), Simulated Doppler radar observations of inhomogeneous clouds: Application to the EarthCARE space mission, *J. Atmos. Oceanic Technol.*, *25*(1), 26–42, doi:10.1175/2007JTECHA956.1.

Schutgens, N. A. J., and D. P. Donovan (2004), Retrieval of atmospheric reflectivity profiles in case of long radar pulses, *J. Atmos. Res.*, *72*, 187–196, doi:10.1016/j.atmosres.2004.03.014.

Stephens, G. L., et al. (2008), CloudSat mission: Performance and early science after the first year of operation, *J. Geophys. Res.*, *113*, D00A18, doi:10.1029/2008JD009982.

Stevens, B., et al. (2003), Dynamics and Chemistry of Marine Stratocumulus: DYCOMS-II, *Bull. Am. Meteorol. Soc.*, *84*(5), 579–593, doi:10.1175/BAMS-84-5-579.

Stokes, G. M., and S. E. Schwartz (1994), The Atmospheric Radiation Measurement (ARM) program: Programmatic background and design of the cloud and radiation test bed, *Bull. Am. Meteorol. Soc.*, *75*(7), 1201–1221, doi:10.1175/1520-0477(1994)075<1201:TARMPP>2.0.CO;2.

Sy, O. O., S. Tanelli, P. Kollias, and Y. Ohno (2014), Application of matched statistical filters for EarthCARE cloud Doppler products, *IEEE Trans. Geosci. Remote Sens.*, *52*(11), 7297–7316, doi:10.1109/TGRS.2014.2311031.

Tanelli, S., E. Im, S. L. Durden, L. Facheris, and D. Giuli (2002), The effects of nonuniform beam filling on vertical rainfall velocity measurements with a spaceborne Doppler radar, *J. Atmos. Oceanic Technol.*, *19*(7), 1019–1034, doi:10.1175/1520-0426(2002)019<1019:TEONBF>2.0.CO;2.

Tanelli, S., S. L. Durden, E. Im, K. S. Pak, D. G. Reinke, P. Partain, J. M. Haynes, and R. T. Marchand (2008), CloudSat's Cloud Profiling Radar after two years in orbit: Performance, calibration, and processing, *IEEE Trans. Geosci. Remote Sens.*, *46*(11), 3560–3573, doi:10.1109/TGRS.2008.2002030.

Uttal, T., and R. A. Kropfli (2001), The effect of radar pulse length on cloud reflectivity statistics, *J. Atmos. Oceanic Technol.*, *18*, 947–961, doi:10.1175/1520-0426(2001)018<0947:TEORPL>2.0.CO;2.

Wang, J., and B. Geerts (2003), Identifying drizzle within marine stratus with W-band radar reflectivity, *Atmos. Res.*, *69*(1-2), 1–27, doi:10.1016/j.atmosres.2003.08.001.

Widener, K., and J. Mead (2004), W-band ARM Cloud Radar—Specification and design, paper presented at Fourteenth ARM Science Team Meeting, U.S. Dep. of Energy, Albuquerque, N. M.

Winker, D. M., M. A. Vaughan, A. Omar, Y. Hu, K. A. Powell, Z. Liu, W. H. Hunt, and S. A. Young (2009), Overview of the CALIPSO mission and CALIOP data processing algorithms, *J. Atmos. Oceanic Technol.*, *96*, 2310–2323, doi:10.1175/2009JTECHA1281.1.

Wood, R. (2012), Stratocumulus clouds, *Mon. Weather Rev.*, *140*(8), 2373–2423, doi:10.1175/MWR-D-11-00121.1.

Wood, R., et al. (2015), Clouds, aerosols, and precipitation in the marine boundary layer: An ARM mobile facility deployment, *Bull. Am. Meteorol. Soc.*, *96*(3), 419–440, doi:10.1175/BAMS-D-13-00180.1.

Zhou, X., P. Kollias, and E. R. Lewis (2015), Clouds, precipitation, and marine boundary layer structure during the MAGIC field campaign, *J. Clim.*, *28*(6), 2420–2442, doi:10.1175/JCLI-D-14-00320.